CHAPTER FOURTEEN

Electron Cryomicroscopy of Biological Macromolecules

RICHARD HENDERSON
Medical Research Council Laboratory of Molecular Biology
Cambridge, United Kingdom

TIMOTHY S. BAKER
Purdue University
Department of Biological Sciences
West Lafayette, Indiana

Contents

1 Macromolecular Structure Determination by Use of Electron Microscopy, **612**
2 Electron Scattering and Radiation Damage, **612**
3 Elastic and Inelastic Scattering, **613**
4 Radiation Damage, **614**
5 Required Properties of Illuminating Electron Beam, **615**
6 Three-Dimensional Electron Cryomicroscopy of Macromolecules, **615**
7 Overview of Conceptual Steps, **616**
8 Classification of Macromolecules, **617**
9 Specimen Preparation, **618**
10 Microscopy, **620**
11 Selection and Preprocessing of Digitized Images, **623**
12 Image Processing and **3D** Reconstruction, **624**
12.1 2D Crystals, **626**
12.2 Helical Particles, **626**
12.3 Icosahedral Particles, **627**
13 Visualization, Modeling, and Interpretation of Results, **628**
14 Trends, **628**
15 Acknowledgments, **628**
16 Abbreviations, **628**

Burger's Medicinal Chemistry and Drug Discovery
Sixth Edition, Volume **1:** Drug Discovery
Edited by Donald **J.** Abraham
ISBN **0-471-27090-3** © **2003** John Wiley & Sons, Inc.

1 MACROMOLECULAR STRUCTURE DETERMINATION BY USE OF ELECTRON MICROSCOPY

The two principal methods of macromolecular structure determination that use scattering techniques are electron microscopy and X-ray crystallography. The most important difference between the two is that the scattering cross section is about 105 times greater for electrons than it is for X-rays, so significant scattering using electrons is obtained for specimens that are 1 to 10 nm thick, whereas scattering or absorption of a similar fraction of an illuminating X-ray beam requires crystals that are 100 to 500 μm thick. The second main difference is that electrons are much more easily focused than X-rays because they are charged particles that can be deflected by electric or magnetic fields. As a result, electron lenses are greatly superior to X-ray lenses and can be used to produce a magnified image of an object as easily as a diffraction pattern. This then allows the electron microscope to be switched back and forth instantly between imaging and diffraction modes so that the image of a single molecule at any magnification can be obtained as conveniently as the electron diffraction pattern of a thin crystal.

In the early years of electron microscopy of macromolecules, electron micrographs of molecules embedded in a thin film of heavy atom stains (1, 2) were used to produce pictures that were interpreted directly. Beginning with the work of Klug and Berger (3), a more rigorous approach to image analysis led first to the interpretation of the two-dimensional (2D) images as the projected density summed along the direction of view and then to the ability to reconstruct the three-dimensional (3D) object from which the images arose (4, 5), with subsequent more sophisticated treatment of image contrast transfer (6).

Later, macromolecules were examined by electron diffraction and imaging without the use of heavy atom stains by embedding the specimens in either a thin film of glucose (7) or in a thin film of rapidly frozen water (8–10), which required the specimen to be cooled while it was examined in the electron microscope. This use of unstained specimens thus led to the structure determination of the molecules themselves rather than the structure of a "negative stain" excluding volume, and has created the burgeoningfield of 3D electron microscopy of macromolecules.

Many medium resolution structures of macromolecular assemblies (e.g., ribosomes), spherical and helical viruses, and larger protein molecules have now been determined by electron cryomicroscopy in ice. Four atomic resolution structures have been obtained by electron cryomicroscopy of thin 2D crystals embedded in glucose, trehalose, or tannic acid (11–14), where specimen cooling reduced the effect of radiation damage. One of these, the structure of bacteriorhodopsin (11)provided the first structure of a seven-helix membrane protein. The medium resolution density distributions can often be interpreted in terms of the chemistry of the structure if a high resolution model of one or more of the component pieces has already been obtained by X-ray, electron microscopy, or NMR methods. As a result, the use of electron microscopy is becoming a powerful technique for which, in some cases, no alternative approach is possible. Useful reviews [e.g., Dubochet et al. (9), Amos et al. (15), Walz and Grigorieff (16), and Baker et al. (17)] and a book [Frank (18)] have been written.

2 ELECTRON SCATTERING AND RADIATION DAMAGE

A schematic overview of scattering and imaging in the electron microscope is depicted in Fig. 14.1. The incident electron beam passes through the specimen and individual electrons are either unscattered or scattered by the atoms of the specimen. This scattering occurs either elastically, with no loss of energy and therefore no energy deposition in the specimen, or inelastically, with consequent energy loss by the scattered electron and accompanying energy deposition in the specimen, resulting in radiation damage. The electrons emerging from the specimen are then

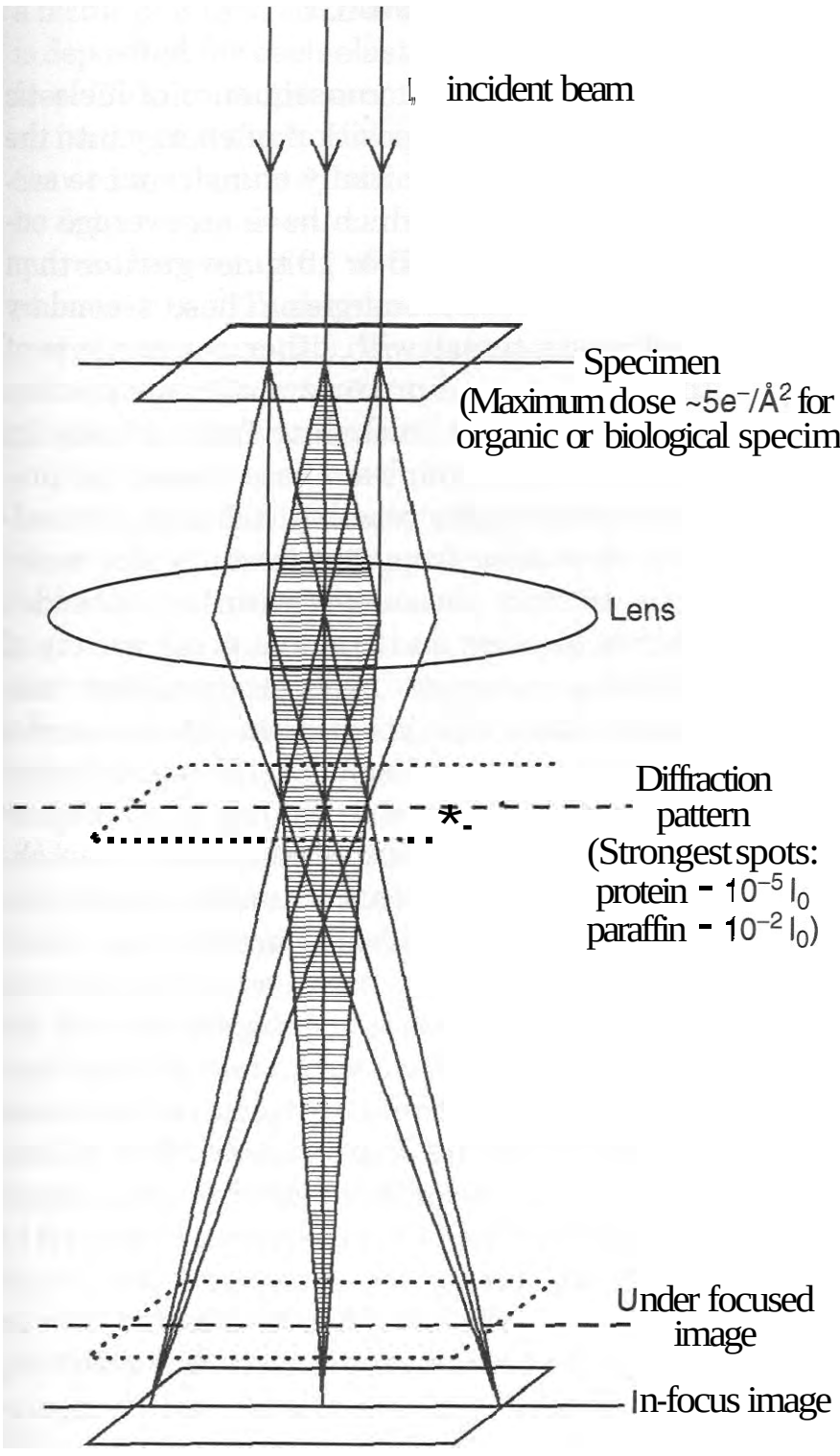


Figure 14.1. Schematic diagram showing the principle of image formation and diffraction in the transmission electron microscope. The incident beam I_0 illuminates the specimen. Scattered and unscattered electrons are collected by the objective lens and focused back to form first an electron diffraction pattern and then an image. For a 2D or **3D** crystal, the electron-diffraction pattern would show a lattice of spots, each of whose intensity is a small fraction of that of the incident beam. In practice, an in-focus image has no contrast, so images are recorded with the objective lens slightly defocused to take advantage of the out-of-focus phase-contrast mechanism.

collected by the imaging optics, shown here for simplicity as a single lens, but in practice consisting of a complex system of five or six lenses, with intermediate images being produced at successively higher magnification at different positions down the column. Finally, in the viewing area, either the electron diffraction pattern or the image can be seen directly by eye on the phosphor screen, or detected by a TV or CCD camera, or recorded on photographic film or image plate.

3 ELASTIC AND INELASTIC SCATTERING

The coherent, elastically scattered electrons contain all the high resolution information describing the structure of the specimen. The amplitudes and phases of the scattered electron beams are directly related to the amplitudes and phases of the Fourier components of the atomic distribution in the specimen. When the scattered beams are recombined with the unscattered beam in the image, they create an interference pattern (the image), which, for thin specimens, is related approximately linearly to the density variations in the specimen. The information about the structure of the specimen can then be retrieved by digitization and computer-based image processing, as described later. The elastic scattering cross sections for electrons are not as simply related to the atomic

composition as happens with X-rays. With X-ray diffraction, the scattering factors are simply proportional to the number of electrons in each atom, normally equal to the atomic number. Given that elastically scattered electrons are in effect diffracted by the electrical potential inside atoms, the scattering factor for electrons depends not only on the nuclear charge but also on the size of the surrounding electron cloud that screens the nuclear charge. As a result, electron scattering factors in the resolution range of interest in macromolecular structure determination (up to 113 $Å^{-1}$), are sensitive to the effective radius of the outer valency electrons and therefore depend sensitively on the chemistry of bonding. Although this is a fascinating field in itself, with interesting work already carried out by the gas phase electron diffraction community [e.g., Hargittai and Hargittai (19)], it is still an area where much work remains to be done. At present, it is probably adequate to think of the density obtained in macromolecular structure analysis by electron microscopy as roughly equivalent to the electron density obtained by X-ray diffraction but with the contribution from hydrogen atoms being somewhat greater relative to carbon, nitrogen, and oxygen.

Those electrons that are inelastically scattered lose energy to the specimen by a number of mechanisms. The energy loss spectrum for a typical biological specimen is dominated by the large cross section for plasmon scattering in the energy range 20–30 eV, with a continuum in the distribution that decreases up to higher energies. At discrete high energies, specific inner electrons in the K shell of carbon, nitrogen, or oxygen can be ejected with corresponding peaks in the energy loss spectrum appearing at 200–400 eV. Any of these inelastic interactions produces an uncertainty in the position of the scattered electron (by Heisenberg's uncertainty principle) and, as a result, the resolution of any information present in the energy loss electron signal extends only to low resolutions of around 15 Å (20). Consequently, the inelastically scattered electrons are generally considered to contribute little except noise to the images.

4 RADIATION DAMAGE

The most important consequence of inelastic scattering is the deposition of energy into the specimen. This is initially transferred to secondary electrons, which have an average energy (20 eV) that is 5 or 10 times greater than the valency bond energies. These secondary electrons interact with other components of the specimen and produce numerous reactive chemical species, including free radicals. In ice-embedded samples, these would be predominantly highly reactive, hydroxyl free radicals that arise from the frozen water molecules. In turn, these react with the embedded macromolecules and create a great variety of radiation products such as modified side chains, cleaved polypeptide backbones, and a host of molecular fragments. From radiation chemistry studies, it is known that thiol or disulfide groups react more quickly than aliphatic groups and that aromatic groups, including nucleic acid bases, are the most resistant. Nevertheless, the end effect of the inelastic scattering is the degradation of the specimen to produce a cascade of heterogeneous products, some of which resemble the starting structure more closely than others. Some of the secondary electrons also escape from the surface of the specimen, causing it to charge up during the exposure. As a rough rule for 100-kV electrons, the dose that can be used to produce an image in which the starting structure at high resolution is still recognizable is about 1 $e^-/Å^2$ for organic or biological materials at room temperature, 5 $e^-/Å^2$ for a specimen near liquid nitrogen temperature (−170°C), and 10 $e^-/Å^2$ for a specimen near liquid helium temperature (4–8 K). However, individual experimenters will often exceed these doses if they wish to enhance the low resolution information in the images that is less sensitive to radiation damage. The effects of radiation damage attributed to electron irradiation are essentially identical to those from X-ray or neutron irradiation for biological macromolecules except for the amount of energy deposition per useful coherent elastically scattered event (21). For electrons scattered by biological structures at all electron energies of interest, the number of inelastic events exceeds the number of elastic events by

a factor of 3 to 4, so that 60 to 80 eV of energy is deposited for each elastically scattered electron. This limits the amount of information in an image of a single biological macromolecule. Consequently, the 3D atomic structure cannot be determined from a single molecule but requires the averaging of the information from at least 10,000 molecules in theory, and even more in practice (21). Crystals used for X-ray or neutron diffraction contain many orders of magnitude more molecules.

It is possible to collect both the elastically and the inelastically scattered electrons simultaneously with an energy analyzer and, if a fine electron beam is scanned over the specimen, then a scanning transmission electron micrograph displaying different properties of the specimen can be obtained. Alternatively, conventional transmission electron microscopes to which an energy filter has been added can be used to select out a certain energy band of the electrons from the image. Both types of microscope can contribute in other ways to the knowledge of structure, but in this presentation, we concentrate on high voltage, phase-contrast electron microscopy of unstained macromolecules most often embedded in ice because this is the method of widest impact in structural biology.

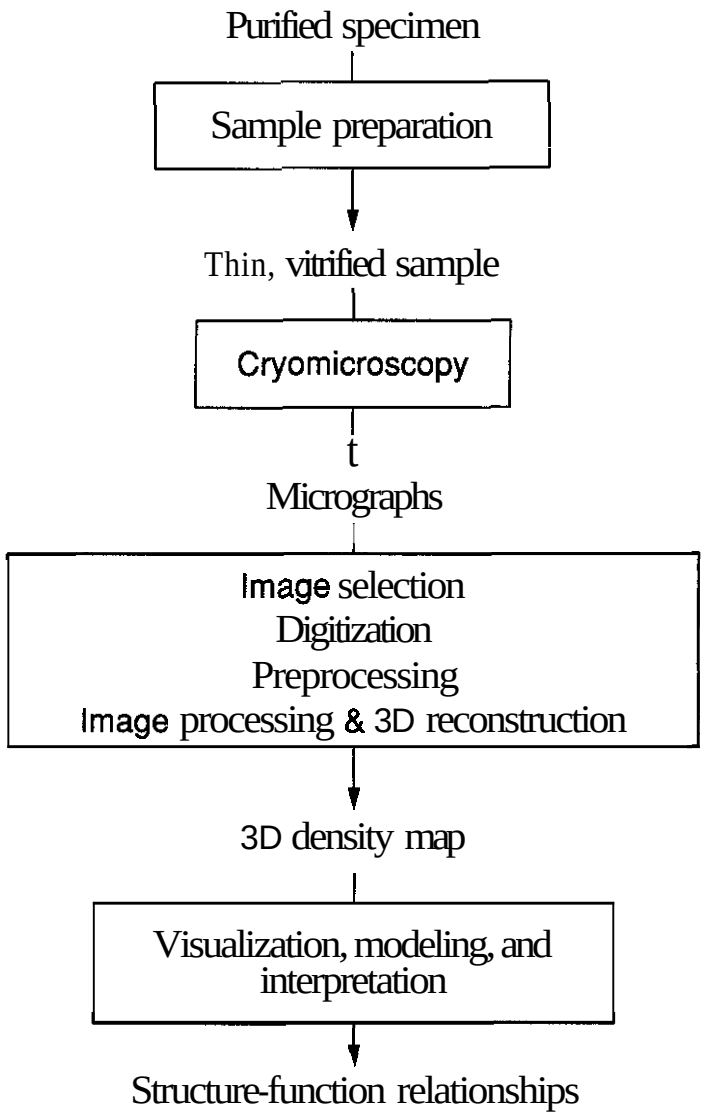


Figure 14.2. Flow diagram showing all the procedures involved in electron cryomicroscopy from sample preparation to map interpretation.

5 REQUIRED PROPERTIES OF ILLUMINATING ELECTRON BEAM

The important properties of the image in terms of defocus, astigmatism, and the presence and effect of amplitude or phase contrast are discussed later. The best quality incident electron beam is produced by a field emission gun (FEG). This is because the electrons from a FEG are emitted from a very small volume at the tip, which is the apparent source size. Once these electrons have been collected by the condenser lens and used to produce the illuminating beam, that beam of electrons is then nearly parallel (divergence of $\sim 10^{-2}$ mrad) and therefore spatially coherent. Similarly, because the emitting tip of a FEG is not heated as much as a conventional thermionic tungsten source, the thermal energy spread of the electrons is relatively small (0.5–1.0 eV) and, as a result, the illuminating beam is closer to being monochromatic. Electron beams can also be produced by a normal, heated tungsten source, which gives a less parallel beam with a larger energy spread, but is nevertheless adequate for electron cryomicroscopy if the highest resolution images are not required.

6 THREE-DIMENSIONAL ELECTRON CRYOMICROSCOPY OF MACROMOLECULES

The determination of 3D structure by cryo-EM methods follows a common scheme for all macromolecules (Fig. 14.2). A more detailed discussion of the individual steps as applied to different classes of macromolecules appears in subsequent sections. Briefly, each specimen must be prepared in a relatively homogeneous, aqueous form (1D or 2D crystals or a suspension of single particles in a limited

number of states) at relatively high concentration, rapidly frozen (vitrified) as a thin film, transferred into the electron microscope, and photographed by means of low dose selection and focusing procedures. The resulting images, if recorded on film, must then be digitized. Digitized images are then processed by the use of computer programs that allow different views of the specimen to be combined into a 3D reconstruction that can be interpreted in terms of other available structural, biochemical, and molecular data.

7 OVERVIEW OF CONCEPTUAL STEPS

Radiation damage by the illuminating electron beam generally allows only one good picture (micrograph) to be obtained from each molecule or macromolecular assembly. In this micrograph, the signal-to-noise ratio of the 2D projection image is normally too small to accurately determine the projected structure. This implies, first, that it is necessary to average many images of different molecules taken from essentially the same viewpoint to increase the signal-to-noise ratio and, second, that many of these averaged projections, taken from different directions, must be combined to build up the information necessary to determine the 3D structure of the molecule. Thus, the two key concepts are: (*1*) averaging to a greater or lesser extent depending on resolution, particle size and symmetry to increase the signal-to-noise ratio; and ***(2)*** the combination of different projections to build a 3D map of the structure.

In addition, there are various technical corrections that must be made to the image data to allow an unbiased model of the structure to be obtained. These include correction for the phase-contrast transfer function (CTF) and, at high resolution, for the effects of beam tilt. For crystals, it is also possible to combine electron diffraction amplitudes with image phases to produce a more accurate structure (7), and in general to correct for loss of high resolution contrast for any reason by "sharpening" the data by application of a negative temperature factor (22).

The idea of increasing the signal-to-noise ratio in electron images of unstained biological macromolecules by averaging was discussed in 1971 (23) and demonstrated in 1975 (7, 24), although earlier work on stained specimens had shown the value of averaging to increase the signal-to-noise ratio. The improvement obtained, as in all repeated measurements, gives a factor of $\sqrt{N}$ improvement in signal-to-noise ratio, where N is the number of times the measurement is made. The effect of averaging to produce an improvement in signal-to-noise ratio is seen most clearly in the processing of images from 2D crystals. Figure 14.3 shows the results of applying a sequence of corrections, beginning with averaging, to two-dimensional crystals of bacteriorhodopsin in 2D space group p3. The panels show: (a, b) 2D averaging, (c) correction for the microscope contrast transfer function (CTF), and (d) threefold crystallographic symmetry averaging of the phases and combination with electron diffraction amplitudes. At each stage in the procedure the projected picture of the molecules gets clearer. The final stage results in a virtually noise-free projected structure for the molecule at near atomic (3Å) resolution.

The earliest successful application of the idea of combining projections to reconstruct the 3D structure of a biological assembly was made by DeRosier and Klug (4). The idea is that each 2D projection corresponds after Fourier transformation to a central section of the 3D transform of the assembly. If enough independent projections are obtained, then the 3D transform will have been fully sampled and the structure can then be obtained by back transformation of the averaged, interpolated, and smoothed 3D transform. This procedure is shown schematically for a three-dimensional object in the shape of a duck, which represents the molecule whose structure is being determined (Fig. 14.4).

In practice, the implementation of these concepts has been carried out in a variety of ways, given that the experimental strategy and type of computer analysis used depend on the type of specimen, especially the molecular weight of the individual molecule, its symmetry, and whether it assembles into an aggregate with one-dimensional (1D), two-dimensional (2D), or three-dimensional (3D) periodic order.

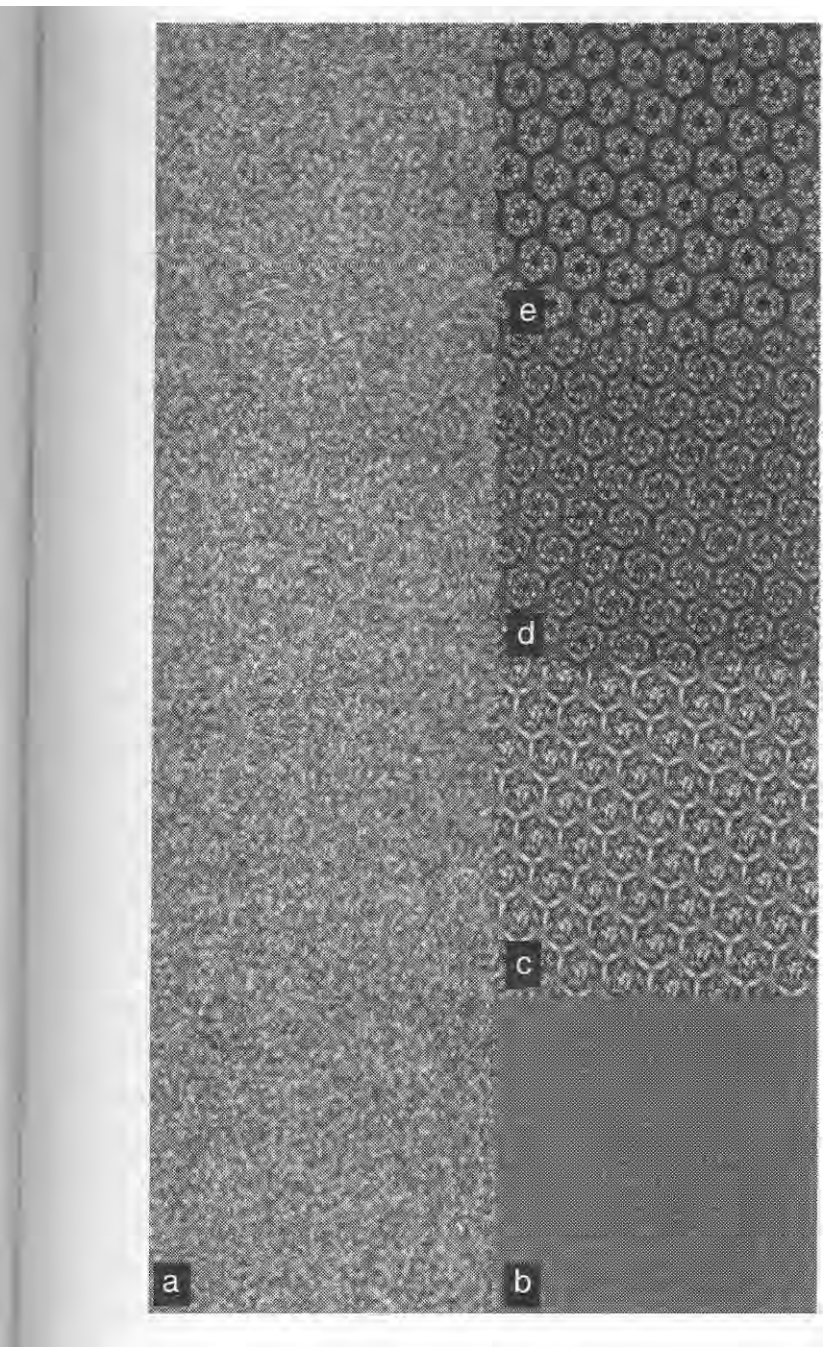


Figure 14.3. Display of the results at different stages of image processing of a digitized micrograph of a 2D crystal of bacteriorhodopsin. The left panel (a) shows an area of the raw digitized micrograph in which only electron noise is visible. The lower right panel (b) shows the results of the averaging of unit cells from the whole picture by unbending in real space and filtering in reciprocal space. The scale of the density in (b) is the same as that in the original micrograph, showing that the signal is very much weaker than the noise. Panel (c) shows the same density as that in (b) but with contrast increased 10-fold to show that the signal in the original picture is approximately 10× below the noise level. Panel (d) shows the density after correction for contrast transfer function (CTF) attributed in this case to a defocus of 6000 Å. Panel (e) shows the density after further threefold crystallographic averaging (the space group is p3) and replacement of image amplitudes by electron diffraction amplitudes. Panel (e) therefore shows an almost perfect atomic resolution image of the projected structure of bacteriorhodopsin. The trimeric rings of molecules are centered on the crystallographic threefold axis and the internal structure shows a-helical segments in the protein.

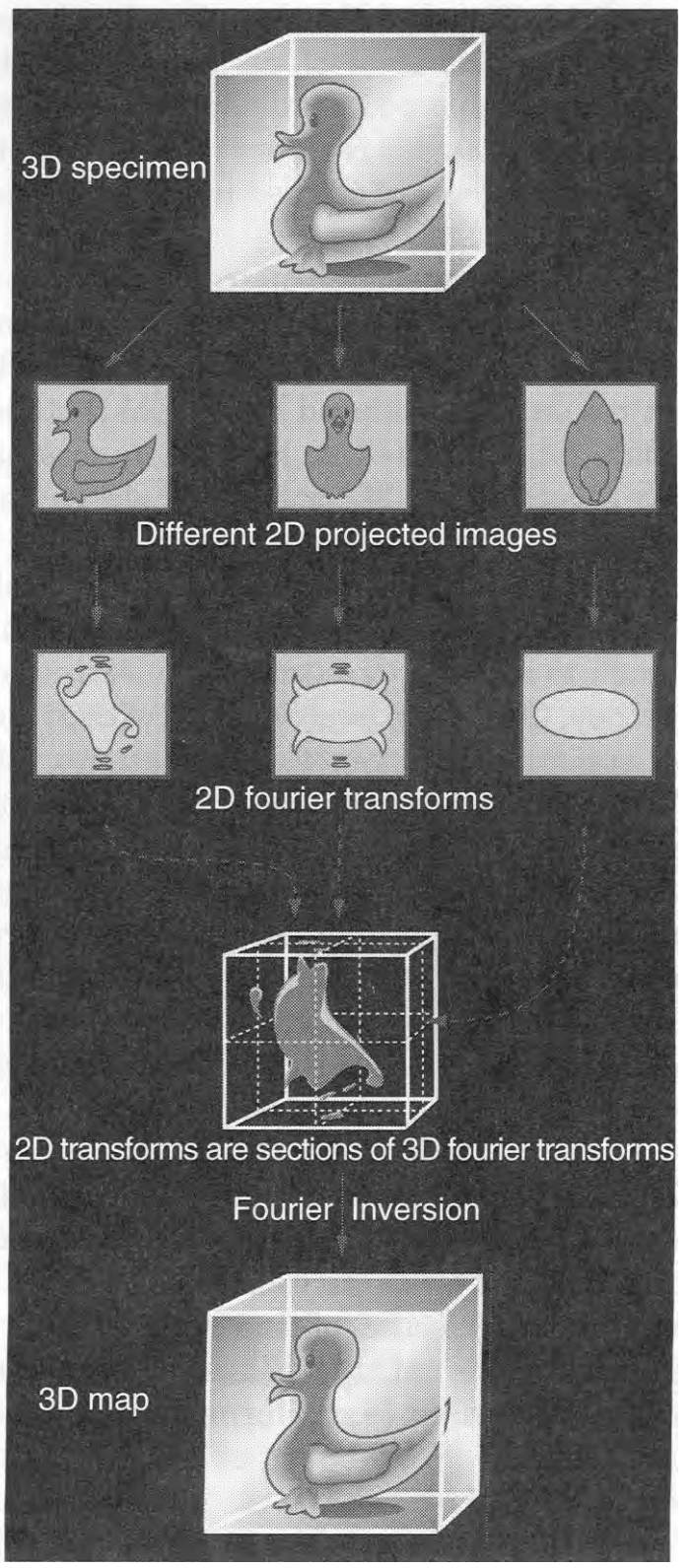


Figure 14.4. Schematic diagram to illustrate the principle of 3D reconstruction. Each 2D projected image, as recorded on the micrograph and after CTF correction, represents a section through the 3D Fourier transform. This is called the projection theorem. After accumulation of enough information from enough different views, a 3D map of the structure can be calculated by Fourier inversion.

8 CLASSIFICATION OF MACROMOLECULES

The symmetry of a macromolecule or supramolecular complex is the primary determinant of how specimen preparation, microscopy, and 3D image reconstruction are

performed. The classification of molecules according to their level of periodic order and symmetry (Table 14.1) provides a logical and convenient way to consider the means by which specimens are studied in 3D by microscopy.

Each type of specimen offers a unique set of challenges in obtaining 3D structural information at the highest possible resolution. The best resolutions achieved by 3D EM methods to date, at about 3–4 Å, have been obtained with several thin, 2D crystals, in large part because of their excellent order.

With the exception of true 3D crystals, which must be sectioned to make them thin enough to study by transmission electron microscopy, the resolutions obtained with biological specimens are generally dictated by the preservation of periodic order, and the symmetry and complexity of the object. Hence, studies of the helical acetylcholine receptor tubes (36), the icosahedral hepatitis B virus capsid (44), the 50S ribosome (45), and the centriole (26) have yielded 3D density maps at resolutions of 4.6, 7.4, 15, and 280 Å, respectively.

If high resolution were the sole objective of EM, it would be necessary, given the capabilities of existing technology, to try to form well-ordered 2D crystals or helical assemblies of each macromolecule of interest. Indeed, a number of different crystallization techniques have been devised [e.g., Horne and Pasquali-Ronchetti (46); Yoshimura et al. (47); Kornberg and Darst (48); Jap et al. (49); Kubalek et al. (50); Rigaud et al. (51); Hasler et al. (52); Reviakine et al. (53); Wilson-Kubalek et al. (54)], and some of these have yielded new structural information about otherwise recalcitrant molecules like RNA polymerase (55). However, despite the obvious technological advantages of having a molecule present in a highly ordered form, most macromolecules function not as highly ordered crystals or helices but instead as single particles (e.g., many enzymes) or, more likely, in concert with other macromolecules as occurs in supramolecular assemblies. Also, crystallization tends to constrain the number of conformational states a molecule can adapt and the crystal conformation might not be functionally relevant. Hence, although resolution may be restricted to much below that realized in the bulk of current X-ray crystallographic studies, cryo-EM methods provide a powerful means to study molecules that resist crystallization in 1D, 2D, or 3D. These methods allow one to explore the dynamic events, different conformational states (as induced, for example, by altering the microenvironment of the specimen), and macromolecular interactions that are the key to understanding how each macromolecule functions.

9 SPECIMEN PREPARATION

The goal in preparing specimens for cryomicroscopy is to keep the biological sample as close as possible to its native state to preserve the structure to atomic or near-atomic resolution in the microscope and during microscopy. The methods by which numerous types of macromolecules and macromolecular complexes have been prepared for cryo-EM studies are now well established (9, 56, 57). Most such methods involve cooling samples at a rate fast enough to permit vitrification (solid, glasslike state) rather than crystallization of the bulk water. Noncrystalline biological macromolecules are typically vitrified by applying a small (often $<10\ \mu L$) aliquot of a purified, approximately 0.2–5 mg/mL suspension of sample to an EM grid coated with a carbon or holey carbon support film. The grid, secured with a pair of forceps and suspended over a container of ethane or propane cryogen slush (maintained near its freezing point by a reservoir of liquid nitrogen), is blotted nearly dry with a piece of filter paper. The grid is then plunged into the cryogen, and the sample, if thin enough ($\sim$0.2 μm or less), is vitrified in millisecond or shorter time periods (58–60).

The ability to freeze samples with a time resolution of milliseconds affords cryo-EM one of its unique and, as yet, perhaps most underutilized advantages: capturing and visualizing dynamic structural events that occur over time periods of a few milliseconds or longer. Several devices that allow samples to be perturbed in a variety of ways as they are plunged into cryogen have been described [e.g., Subramaniarn et al. (61); Berriman and Unwin (59); Siegel et al. (62); Trachtenberg (63); White et

Table 14.1 Classification of Macromolecules According to Periodic Order and Symmetry

Periodic Order	Type Symmetry		Example Macromolecule/Complex	Representative Reference
0D	Point group	C_1	Ribosome	25
		C_1	Centriole	26
		C_5	BacteriophageΦ29 head	27
		C_8	Ribonucleoprotein vault	28
		C_{17}	TMV disk	29
		D_2	β-galactosidase	30
		D_8	Clathrin coats	31
		D_6	*Lumbricus terrestris* hemoglobin	32
		T	Dps protein	33
		O	*Azotobacter* pyruvate dehydrogenase core	34
		I	Icosahedral viruses	17
1D	Screw axis (helical)"		Acto-myosin filament	35
			Acetylcholine receptor tubes	36
			Microtubule	37
			Bacterial flagella	38
			Tobacco mosaic virus	39
2D	2D space group (2D crystal)	p3	Bacterial rhodopsin membrane	11
		$p42_12$	Aquaporin membrane	40
		p6	Gap junction membrane	41
		p321	Light harvesting complex II	12
		$p12_1$	Tubulin sheet	13
3D	3D space group (3D crystal)	$P2_12_12_1$	Myosin S1 protein crystal	42
		$P6_5$ or $P6_4$	Insect flight muscle	43

"The symmetry of a helical structure is defined by an n_m space axis, which combines a rotation of $2\pi/n$ radius about an axis followed by a translation of m/n of the repeat distance.

al. (60)]. Examples of the use of such devices include spraying acetylcholine onto its receptor to cause the receptor channel to open (64), or lowering the pH of an enveloped virus sample to initiate early events of viral fusion (65), or inducing a temperature jump with a flash-tube system to study phase transitions in liposomes (66), or mixing myosin S1 fragments with F-actin to examine the geometry of the crossbridge powerstroke in muscle (67).

Crystalline (2D) samples fortunately can often be prepared for cryo-EM by means of simpler procedures, and vitrification of the bulk water is not always essential to achieve success (68). Such specimens may be applied to the carbon film on an EM grid by normal adhesion methods, washed with 1–2% solutions of solutes like glucose, trehalose, or tannic acid, blotted gently with filter paper to remove excess solution, air dried, loaded into a cold holder, inserted into the microscope, and, finally, cooled to liquid nitrogen temperature.

10 MICROSCOPY

Once the vitrified specimen is inserted into the microscope and sufficient time is allowed (−15 min) for the specimen stage to stabilize to minimize drift and vibration, microscopy is performed to generate a set of images that, with suitable processing procedures, can later be used to produce a reliable 3D reconstruction of the specimen at the highest possible resolution. To achieve this goal, imaging must be performed at an electron dose that minimizes beam-induced radiation damage to the specimen, with the objective lens of the microscope defocused to enhance phase contrast from the weakly scattering, unstained biological specimen, and under conditions that keep the specimen below the devitrification temperature and minimize its contamination.

The microscopist locates specimen areas suitable for photography by searching the EM grid at very low magnification (≤3000×) to keep the irradiation level very low (<0.05 $e^-/Å^2$) while assessing sample quality. In microscopes operated at 200 keV or higher, where image contrast is very weak, it is helpful to perform the search procedure with the assistance of a CCD camera or a video-rate TV-intensified camera system. For some specimens, like thin 2D crystals, searching is conveniently performed by viewing the low magnification, high contrast image produced by slightly defocusing the electron diffraction pattern by use of the diffraction lens.

After a desired specimen area is identified, the microscope is switched to high magnification mode for focusing and astigmatism correction. These adjustments are typically performed in a region about 2–10 μm away from the chosen area at the same or higher magnification than that used for photography. The choice of magnification, defocus level, accelerating voltage, beam coherence, electron dose, and other operating conditions is dictated by several factors. The most significant ones are the size of the particle or crystal unit cell being studied, the anticipated resolution of the images, and the requirements of the image processing needed to compute a 3D reconstruction to the desired resolution. For most specimens at required resolutions from 3 to 30 Å, images are typically recorded at 25,000–50,000× magnification, with an electron dose of between 5 and 20 $e^-/Å^2$. These conditions yield micrographs of sufficient optical density (OD 0.2–1.5) and image resolution for subsequent image-processing steps. Most modern EMs provide some mode of low dose operation for imaging beam-sensitive, vitrified biological specimens.

The intrinsic low contrast of unstained specimens makes it impossible to observe and focus on specimen details directly, as is routine with stained or metal-shadowed specimens. Focusing, aimed to enhance phase contrast in the recorded images but minimize beam damage to the desired area, is achieved by judicious defocusing on a region that is adjacent to the region to be photographed and preferably situated on the microscope tilt axis. The appropriate focus level is set by adjusting the appearance of either the Fresnel fringes that occur at the edges of holes in the carbon film or the "phase granularity" from the carbon support film.

Unfortunately, electron images do not give a direct rendering of the specimen density distribution. The relationship between image and specimen is described by the contrast transfer function (CTF), which is characteris-

tic of the particular microscope used, the specimen, and the conditions of imaging. The microscope CTF arises from the objective lens focal setting and from the spherical aberration present in all electromagnetic lenses and varies with the defocus and accelerating voltage according to a formula (see below) that includes both phase- and amplitude-contrast components. First, however, it might be useful to describe briefly the essentials of amplitude contrast and phase contrast, two concepts carried over from optical microscopy. Amplitude contrast refers to the nature of the contrast in an image of an object that absorbs the incident illumination or scatters it in any other way, so that a proportion of it is lost. As a result, the image appears darker where greater absorption occurs. Phase contrast is required if an object is transparent (i.e., it is a pure phase object) and does not absorb but only scatters the incident illumination. Biological specimens for cryo-EM are almost pure phase objects and the scattering is relatively weak, so that the simple theory of image formation by a weak phase object applies (69, 70). An exactly in-focus image of a phase object has no contrast variation because all the scattered illumination is focused back to equivalent points in the image of the object from which it was scattered. In optical microscopy, the use of a quarter wave plate can retard the phase of the direct unscattered beam, so that an in-focus image of a phase object has very high "Zernicke" phase contrast. However, there is as yet no simple quarter wave plate for electrons, so instead, phase contrast is created by introducing phase shifts into the diffracted beams by adjustment of the excitation of the objective lens so that the image is slightly defocused. In addition, because all matter is composed of atoms and the electric potential inside each atom is very high near the nucleus, even the electron scattering behavior of the light atoms found in biological molecules deviates from that of a weak phase object; however, for a deeper discussion of this the reader should refer to Reimer (70) or Spence (69). In practice, the proportion of "amplitude" contrast is about 7% at 100 kV, 5% at 200 kV, and 4% at 300 kV for low dose images of protein molecules embedded in ice.

The overall dependency of CTF on resolution, wavelength, defocus, and spherical aberration is given by

$$CTF(\nu) = -\{(1 - F_{\text{amp}}^2)^{1/2}\sin[\chi(\nu)] + F_{\text{amp}}\cos[\chi(\nu)]\}$$

where $\chi(\nu) = \pi\lambda\nu^2(\Delta f - 0.5C_s\lambda^2\nu^2)$; v is the spatial frequency (in Å^{-1}); F_{amp} is the fraction of amplitude contrast; λ is the electron wavelength (in &, where

$$\lambda = 12.3/\sqrt{V + 0.000000978 \cdot V^2}$$

(=0.037, 0.025, and 0.020 Å for 100, 200, and 300 keV electrons, respectively); V is the voltage (in volts); Δf is the underfocus (in &; and C_s is the spherical aberration of the objective lens of the microscope (in Å).

In addition, this CTF is attenuated by an envelope or damping function, which depends on the coherence of the beam, specimen drift, and other factors (6, 71, 72). Figure 14.5 shows a few representative CTFs for different amounts of defocus on a normal and a FEG microscope. Thus, for a particular defocus setting of the objective lens, phase contrast in the electron image is positive and maximal only at a few specific spatial frequencies. Contrast is either lower than maximal, completely absent, or it is opposite (inverted or reversed) from that at other frequencies. Hence, as the objective lens is focused, the electron microscopist selectively accentuates image details of a particular size.

Images are typically recorded 0.8–3.0 μm underfocus to enhance specimen features in the 20–40 Å size range and thereby facilitate phase origin and specimen orientation search procedures carried out in the image-processing steps. However, this level of underfocus also enhances the contrast envelope in lower resolution maps, which may help in interpretation. To obtain results at better than 10–15 Å resolution, it is essential to record, process, and combine data from several micrographs that span a range of defocus levels [e.g., Unwin and Henderson (7); Bottcher et al. (44)]. This strategy ensures good information transfer at all spatial frequencies up to the limiting reso-

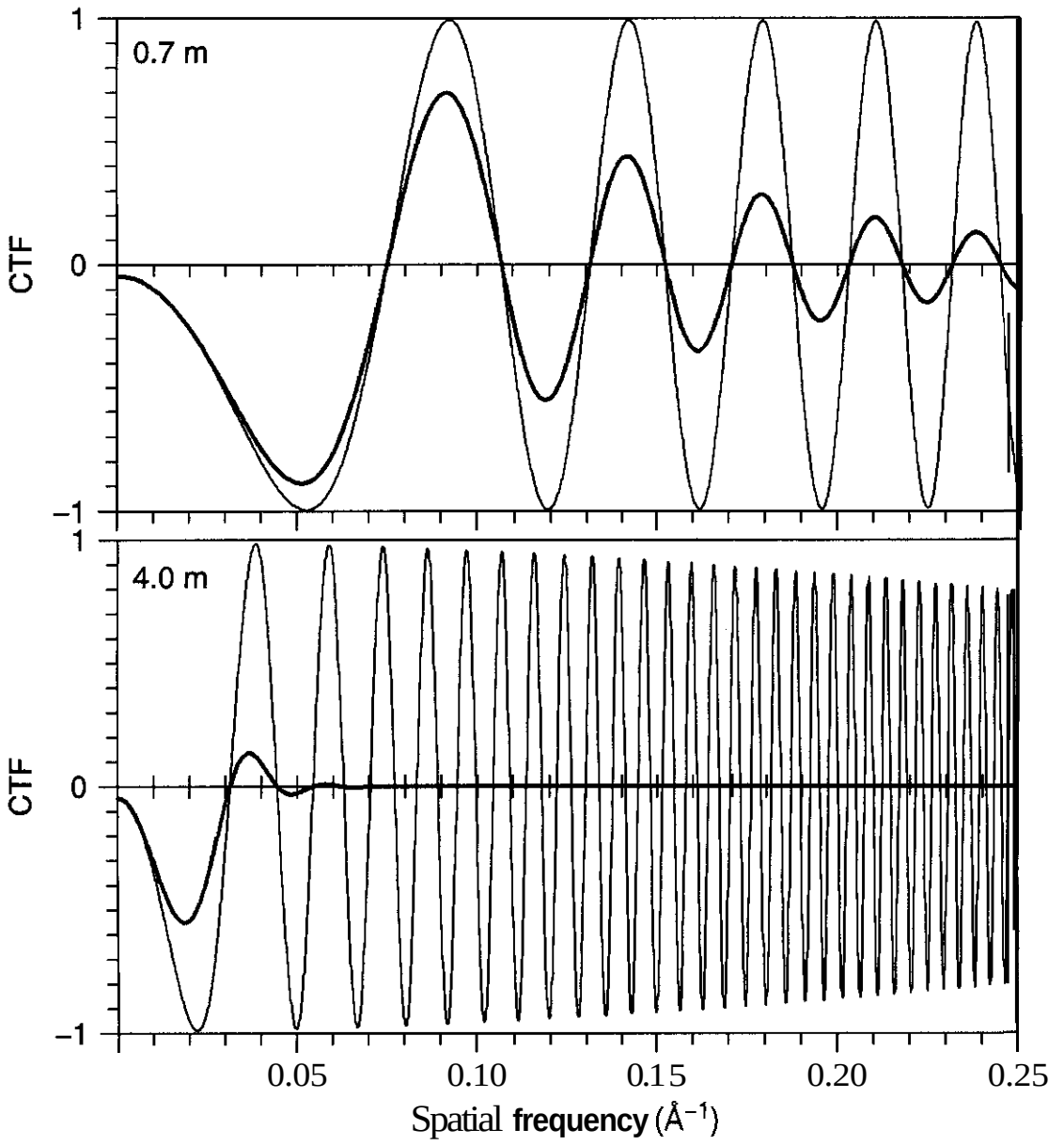


Figure 14.5. Representative plots of the contrast transfer function (CTF) as a function of spatial frequency, for two different defocus settings (0.7 and 4.0 μm underfocus) and for a field emission (light curve) or tungsten (dark curve) electron source. All plots correspond to electron images formed in an electron microscope operated at 200 kV and with objective lens aberration coefficients, $C_s = C_c = 2.0$ mm, and assuming amplitude contrast of 4.8% (73). The spatial coherence, which is related to the electron source size and expressed as β, the half-angle of illumination, for tungsten and FEG electron sources was fixed at 0.3 and 0.015 milliradians, respectively. Likewise, the temporal coherence (expressed as ΔE, the energy spread) was fixed at 1.6 and 0.5 eV for tungsten and FEG sources. The combined effects of the poorer spatial and temporal coherence of the tungsten source leads to a significant dampening, and hence loss of contrast, of the CTF at progressively higher resolutions compared to that observed in FEG-equipped microscopes. The greater number of contrast reversals with higher defocus arises because of the greater out-of-focus phase shifts.

lution but requires careful compensation for the effects of the microscope CTF during image processing. Also, the recording of image focal pairs or focal series from a given specimen area can be beneficial in determining origin and orientation parameters for processing of images of single particles [e.g., Cheng et al. (74); Trus et al. (75)].

Many high resolution cryo-EM studies are now performed with microscopes operated at 200 keV or higher and with field emission gun (FEG) electron sources [e.g., Zemlin (76, 78); Zhou and Chiu (77); Mancini et al. (79)]. The high coherence of a FEG source ensures that phase contrast in the images remains strong out to high spatial frequencies (>1/3.5 $Å^{-1}$), even for highly defocused images. The use of higher voltages provides potentially higher resolution [greater depth of field (i.e., less curvature of the Ewald sphere) attributed to smaller electron beam wavelength], better beam penetration (less multiple scattering),

reduced problems with specimen charging that plague microscopy of unstained or uncoated vitrified specimens (80), and reduced phase shifts associated with beam tilt.

Images are recorded on photographic film or on a CCD camera with either flood beam or spot-scan procedures. Film, with its advantages of low cost, large field of view, and high resolution (−10 μm), has remained the primary image recording medium for most cryo-EM applications, despite disadvantages of high background fog and need for chemical development and digitization. CCD cameras provide image data directly in digital form and with very low background noise, but suffer from higher cost, limited field of view, limited spatial resolution caused by poor point spread characteristics, and a fixed pixel size (typically between 14 and 24 μm). They are useful, for example, for precise focusing and adjustment of astigmatism [e.g., Krivanek and Mooney (81); Sherman et al. (82)].

For studies in which specimens must be tilted to collect 3D data, such as with 2D crystals, or single particles that adopt preferred orientations on the EM grid, or specimens requiring tomography, microscopy is performed in essentially the same way as described above. However, the limited tilt range (±60–70°) of most microscope goniometers can lead to nonisotropic resolution in the 3D reconstructions (the "missing cone" problem), and tilting generates a constantly varying defocus across the field of view in a direction normal to the tilt axis. The effects caused by this varying defocus level must be corrected in high resolution applications.

11 SELECTION AND PREPROCESSING OF DIGITIZED IMAGES

Before any image analysis or classification of the molecular images can be done, a certain amount of preliminary checking and normalization is required to ensure there is a reasonable chance that a homogeneous population of molecular images has been obtained. First, good quality micrographs are selected in which the electron exposure is correct, there is no image drift or blurring, and there is minimal astigmatism and a reasonable amount of defocus to produce good phase contrast. This is usually done by visual examination and optical diffraction.

Once the best pictures have been chosen, the micrographs must be scanned and digitized on a suitable densitometer. The sizes of the steps between digitization of optical density and the size of the sample aperture over which the optical density is averaged by the densitometer must be sufficiently small to sample the detail present in the image at fine enough intervals (83). Normally, a circular (or square) sample aperture of diameter (or length of side) equal to the step between digitizations is used. This avoids digitizing overlapping points, without missing any of the information recorded in the image. The size of the sample aperture and digitization step depends on the magnification selected and the resolution required. A value of 1/4 to 1/3 of the required limit of resolution (measured in μm on the emulsion) is normally ideal because it avoids having too many numbers (and therefore wasting computer resources), without losing anything during the measurement procedure. For a 40,000× image, on which a resolution of 10 Å at the specimen is required, a step size of 10 μm {= ¼ × [(10 Å × 40,000)/(10,000 Å/μm)]} would be suitable.

The best area of an image of a helical or 2D crystal specimen can then be boxed off using a soft-edge mask. For images of single particles, a stack of individual particles can be created by selecting out many small areas surrounding each particle. Because, in the later steps of image processing, the orientation and position of each particle are refined by comparing the amplitudes and phases of their Fourier components, it is important to remove spurious features around the edge of each particle and to make sure the different particle images are on the same scale. This is normally done by masking off a circular area centered on each particle and floating the density so that the average around the perimeter becomes zero (83). The edge of the mask is apodized by applying a soft cosine bell shape to the original densities so they taper toward the background level. Finally, to compensate for variations in the exposure attributed to ice thickness or electron dose, most microscopists normalize the stack of individual particle images so that

the mean density and mean density variation over the field of view are set to the same values for all particles (84).

Once some good particles or crystalline areas for 1D or 2D crystals have been selected, digitized, masked, and their intensity values normalized, true image processing can begin.

12 IMAGE PROCESSING AND 3D RECONSTRUCTION

Although the general concepts of signal averaging, together with combining different views to reconstruct the 3D structure, are common to the different computer-based procedures that have been implemented, it is important to emphasize one or two preliminary points. First, a homogeneous set of particles must be selected for inclusion in the 3D reconstruction. This selection may be made by eye, to eliminate obviously damaged particles or impurities, or by the use of multivariate statistical analysis (85) or some other classification scheme. This allows a subset of the particle images to be used to determine the structure of a better defined entity. All image-processing procedures require the determination of the same parameters that are needed to specify unambiguously how to combine the information from each micrograph or particle. These parameters are: the magnification, defocus, astigmatism, and, at high resolution, the beam tilt for each micrograph; the electron wavelength used (i.e., accelerating voltage of the microscope); the spherical aberration coefficient (C_s) of the objective lens; and the orientation and phase origin for each particle or unit cell of the 1D, 2D, or 3D crystal. There are 13 parameters for each particle, of which eight may be common to each micrograph and two or three (C_s, kV, magnification) to each microscope. The different general approaches that have been used in practice to determine the 3D structure of different classes of macromolecular assemblies from one or more electron micrographs are listed in Table 14.2.

The precise way in which each general approach codes and determines the particle or unit cell parameters varies greatly and is not described in detail. Much of the computer software used in image reconstruction studies is relatively specialized compared to that used in the more mature field of macromolecular X-ray crystallography. In part, this may be attributed to the large diversity of specimen types amenable to cryo-EM and reconstruction methods. As a consequence, image-reconstruction software is evolving quite rapidly, and references to software packages cited in Table 14.2 are likely to become quickly outdated. Extensive discussion of algorithms and software packages in use at this time may be found in a number of recent special issues of the *Journal of Structural Biology* [volumes 116(1), 120(3), 121(2), and 125(2/3)].

In practice, attempts to determine or refine some parameters may be affected by the inability to determine accurately one of the other parameters. The solution of the structure is therefore an iterative procedure in which reliable knowledge of the parameters that describe each image is gradually built up to produce an increasingly accurate structure, until no more information can be squeezed out of the micrographs. At this point, if any of the origins or orientations is wrongly assigned, there will be a loss of detail and signal-to-noise ratio in the map. If a better determined or higher resolution structure is required, it would then be necessary to record images on a better microscope or to prepare new specimens and record better pictures.

The reliability and resolution of the final reconstruction can be measured by use of a variety of indices. For example, the differential phase residual (DPR) (133), the Fourier shell correlation (FSC) (134), and the Q-factor (135) are three such measures. DPR is the mean phase difference, as a function of resolution, between the structure factors from two independent reconstructions, often calculated by splitting the image data into two halves. FSC is a similar calculation of the mean correlation coefficient between the complex structure factors of the two halves of the data as a function of resolution. The Q-factor is the mean ratio of the vector sum of the individual structure factors from each image divided by the sum of their moduli, again calculated as a function of resolution. Perfectly accurate measurements would have values of DPR, FSC, and Q-factor of 0°, 1.0, and 1.0 respectively, whereas random data containing no informa-

Table 14.2 Methods of Three-Dimensional Image Reconstruction

Type Structure (symmetry)	Method	Reference(s) to Technical/ Theoretical Details
Asymmetric (Point group C_1)	Random conical tilt	18, 87, 88
	•Software package	89
	Angular reconstitution	32, 90
	*Software package	91
	Weighted back projection	92, 93
	Radon transform alignment	94
	Reference-based alignment	95
	Reference free alignment	96, 97
	Fourier reconstruction and alignment	98
	Tomographic tilt series and remote control of microscope[a]	99–102
Symmetric (Point groups C_n, D_n; $n > 1$)	Angular reconstitution	32, 90
	*Software packages	91, 103
	Fourier–Bessel synthesis	27
	Reference-based alignment and weighted back projection	104
Icosahedral (Point group I)	Fourier–Bessel synthesis (common-lines)	79, 105–107
	*Reference-based alignment	108–111
	*Software packages	112–116
	Angular reconstitution	90, 117
	Tomographic tilt series	
Helical	Fourier–Bessel synthesis	4, 36, 83, 119–123
	•Software packages and filament straightening routines	112, 123–126
2D Crystal	Random azimuthal tilt	11, 15, 24, 127, 128
	*Software packages	112, 129
3D Crystal	Oblique section reconstruction	43, 130
	*Software package	131
	Sectioned 3D crystal	42

"Note: Electron tomography is the subject of an entire issue of *J*. Struct. Biol. [120, 207–395 (1997)] and a book edited by Frank (132).

tion would have values of 90°, 0.0, and 0.0. The spectral signal-to-noise ratio (SSNR) criterion has been advocated as the best of all (136): it effectively measures, as a function of resolution, the overall signal-to-noise ratio (squared) of the whole of the image data. It is calculated by taking into consideration how well all the contributing image data agree internally.

An example of a typical strategy for determination of the 3D structure of a new and unknown molecule without any symmetry and that does not crystallize might be as follows:

1. Record a single axis tilt series of particles embedded in negative stain, with a tilt range from −60" to +60".
2. Calculate 3D structures for each particle by use of an R-weighted back-projection algorithm (93).
3. Average 3D data for several particles in real or reciprocal space to get a reasonably good 3D model of the stain excluding the region of the particle.
4. Record a number of micrographs of the particles embedded in vitreous ice.
5. Use the 3D negative stain model obtained in (3) with inverted contrast to determine the rough alignment parameters of the particle in the ice images.
6. Calculate a preliminary 3D model of the average, ice-embedded structure.

7. Use the preliminary 3D model to determine more accurate alignment parameters for the particles in the ice images.
8. Calculate a better 3D model.
9. Determine defocus and astigmatism to allow CTF calculation and correct 3D model so that it represents the structure at high resolution.
10. Keep adding pictures at different defocus levels to get an accurate structure at as high a resolution as possible.

For large single particles with no symmetry or for particles with higher symmetry or for crystalline arrays, it should be possible to miss out the negative staining steps and go straight to alignment of particle images from ice-embedding because the particle or crystal tilt angles can be determined internally from comparison of phases along common lines in reciprocal space or from the lattice or helix parameters from a 2D or 1D crystal.

The following discussion briefly outlines for a few specific classes of macromolecule the general strategy for carrying out image processing and 3D reconstruction (see Fig. 14.6).

12.1 2D Crystals

For 2D crystals, the general 3D reconstruction approach consists of the following steps: First, a series of micrographs of single 2D crystals are recorded at different tilt angles, with random azimuthal orientations. Each crystal is then unbent using cross-correlation techniques, to identify the precise position of each unit cell (127), and amplitudes and phases of the Fourier components of the average of that particular view of the structure are obtained for the transform of the unbent crystal. The reference image used in the cross-correlation calculation can either be a part of the whole image masked off after a preliminary round of averaging by reciprocal space filtering of the regions surrounding the diffraction spots in the transform, or it can be a reference image calculated from a previously determined 3D model. The amplitudes and phases from each image are then corrected for the CTF and beam tilt (11,22, 127) and merged with data from many other crystals by scaling and origin refinement, taking into account the proper symmetry of the 2D space group of the crystal. Finally, the whole data set is fitted by least squares to constrained amplitudes and phases along the lattice lines (137) before calculating a map of the structure. The initial determination of the 2D space group can be carried out by a statistical test of the phase relationships in one or two images of untilted specimens (138). The absolute hand of the structure is automatically correct, given that the 3D structure is calculated from images whose tilt axis and tilt angle are known. Nevertheless, care must be taken not to make any of a number of trivial mistakes that would invert the hand.

12.2 Helical Particles

The basic steps involved in processing and 3D reconstruction of helical specimens include: Recording a series of micrographs of vitrified particles suspended over holes in a perforated carbon support film. The micrographs are digitized and Fourier-transformed to determine image quality (astigmatism, drift, defocus, presence, and quality of layer lines, etc.). Individual particle images are boxed, floated, and apodized within a rectangular mask. The parameters of helical symmetry (number of subunits per turn and pitch) must be determined by indexing the computed diffraction patterns. If necessary, simple spline-fitting procedures may be employed to "straighten" images of curved particles (124), and the image data may be reinterpolated (126) to provide more precise sampling of the layer line data in the computed transform. Once a preliminary 3D structure is available, a much more sophisticated refinement of all the helical parameters can be used to unbend the helices onto a predetermined average helix so that the contributions of all parts of the image are correctly treated (123). The layer line data are extracted from each particle transform and two phase origin corrections are made, one to shift the phase origin to the helix axis (at the center of the particle image) and the other to correct for effects caused by having the helix axis tilted out of the plane normal to the electron beam in the electron microscope. The layer line data are separated out into near- and far-side data, corresponding to contributions from the near and far sides of each particle imaged. The relative rotations and

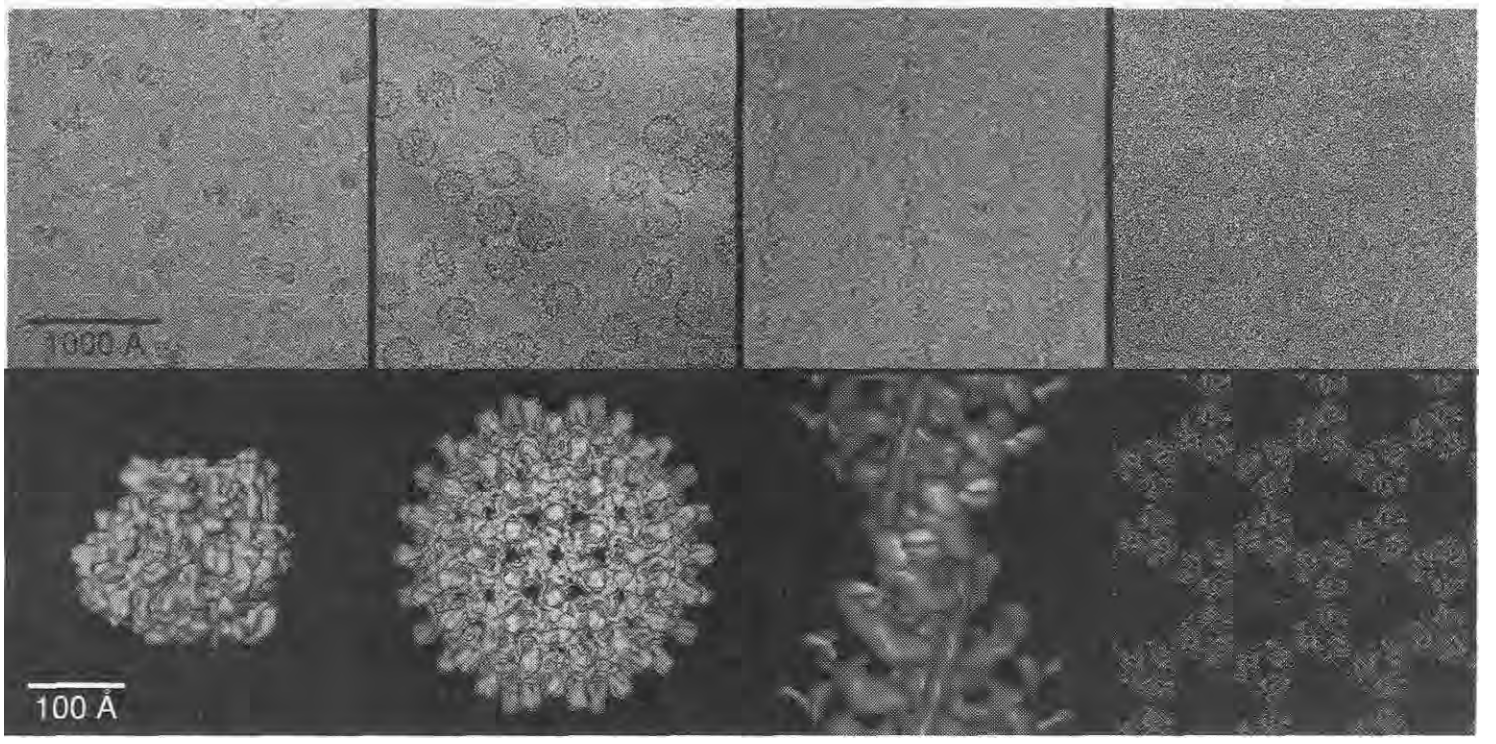


Figure 14.6. Examples of macromolecules studied by cryo-EM and 3D image reconstruction and the resulting 3D structures (bottom row) after cryo-EM analysis. All micrographs (top row) are displayed at about 170,000× magnification and all models at about 1,200,000× magnification. (a) A single particle without symmetry: The micrograph shows 70S E. *coli* ribosomes complexed with mRNA and fMet-tRNA. The surface-shaded density map, made by averaging 73,000 ribosome images from 287 micrographs has a resolution (FSC) of 11.5 Å. The 50S and 30S subunits and the tRNA are colored blue, yellow, and green, respectively. The identity of many of the subunits is known and some RNA double helices are clearly recognizable by their major and minor grooves (e.g., helix 44 is shown in red). [Courtesy of J. Frank (SUNY, Albany), using data from Gabashvili et al. (86).] (b) A single particle with symmetry: The micrograph shows hepatitis B virus cores. The 3D reconstruction, at a resolution of 7.4 Å (DPR), was computed from 6384 particle images taken from 34 micrographs. [From Bottcher et al. (44).] (c) A helical filament: The micrograph shows actin filaments decorated with myosin S1 heads containing the essential light chain. The 3D reconstruction, at a resolution of 30–35 Å, is a composite in which the differently colored parts are derived from a series of difference maps that were superimposed on f-actin. The components include: f-actin (blue), myosin heavy chain motor domain (orange), essential light chain (purple), regulatory light chain (white), tropomyosin (green), and myosin motor domain N-terminal beta-barrel (red). [Courtesy of A. Lin, M. Whittaker, and R. Milligan (Scripps Research Institute, La Jolla, CA).] (d) A 2D crystal, light-harvesting complex LHCII at 3.4-Å resolution. The model shows the protein backbone and the arrangement of chromophores in a number of trimeric subunits in the crystal lattice. In this example, image contrast is too low to see any hint of the structure without image processing (see also Fig. 14.3). See color insert. [Courtesy of W. Kuhlbrandt (Max-Planck-Institute for Biophysics, Frankfurt, Germany).]

translations needed to align the different transforms are determined so the data may be merged and a 3D reconstruction computed by Fourier-Bessel inversion procedures (83). Determination of the absolute hand requires comparison of a pair of images recorded with a small tilt of the specimen between the views (139).

12.3 Icosahedral Particles

The typical strategy for processing and 3D reconstruction of icosahedral particles consists of the following steps: First, a series of micrographs of a monodisperse distribution of particles, normally suspended over holes in a perforated carbon support film, is recorded. After digitization of the micrographs, individual particle images are boxed and floated with a circular mask. The astigmatism and defocus of each micrograph is measured from the sum of intensities of the Fourier transforms of all particle images (140). Autocorrelation techniques are then used to estimate the particle phase origins, which coincide with the center of each particle, where all rotational symmetry axes intersect (141). The view orientation

of each particle, defined by three Eulerian angles, is determined either by means of common and cross-common lines techniques or with the aid of model-based procedures [e.g., Crowther (106); Fuller et al. (107); Baker et al. (17)]. Once a set of self-consistent particle images is available, an initial, low resolution 3D reconstruction is computed by merging these data with Fourier-Bessel methods (106). This reconstruction then serves as a reference for refining the orientation, origin, and CTF parameters of each of the included particle images, for rejecting "bad" images, and for increasing the size of the data set by including new particle images from additional micrographs taken at different defocus levels. A new reconstruction, computed from the latest set of images, serves as a new reference and the above refinement procedure is repeated until no further improvements, as measured by the reliability criteria mentioned above, are made. Determination of the absolute hand of the structure requires the recording and processing of a pair of images taken with a known, small relative tilt of the specimen between the two views (142).

13 VISUALIZATION, MODELING, AND INTERPRETATION OF RESULTS

Once a reliable 3D map is obtained, computer graphics and other visualization tools may be used as aids in interpreting morphological details and understanding biological function in the context of biochemical and molecular studies and complementary X-ray crystallographic and other biophysical measurements.

14 TRENDS

The new generation of intermediate voltage (~300 kV) FEG microscopes is now making it much easier to obtain higher resolution images that, by use of larger defocus values, have good image contrast at both very low and very high resolution. The greater contrast at low resolution greatly facilitates particle-alignment procedures, and the increased contrast resulting from the high coherence illumination helps to increase the signal-to-noise ratio for the structure at high resolution. Cold stages are constantly being improved, with several liquid helium stages now in operation (143, 144). Two of these are commercially available from JEOL and FEI/Philips.

Finally, three additional likely trends include: (1) increased automation, including the recording of micrographs, the use of spotscan procedures in remote microscope operation (145, 146), and in every aspect of image processing; (2) production of better electronic cameras (e.g., CCD or pixel detectors); and (3) increased use of dose-fractionated, tomographic tilt series, to extend EM studies to the domain of larger supramolecular and cellular structures (102, 147).

15 ACKNOWLEDGMENTS

We are greatly indebted to all our colleagues at Purdue and Cambridge for their insightful comments and suggestions; to B. Bottcher, R. Crowther, J. Frank, W. Kiihlbrandt, and R. Milligan for supplying images used in Figure 14.6; and J. Brightwell for editorial assistance. T.S.B. was supported in part by Grant GM33050 from the National Institutes of Health.

16 ABBREVIATIONS

0D	zero-dimensional (single particles)
1D	one-dimensional (helical)
2D	two-dimensional
3D	three-dimensional
CCD	charge coupled device (slow scan TV detector)
cryo-EM	electron cryomicroscopy
CTF	contrast transfer function
EM	electron microscope/microscopy
FEG	field emission gun

REFERENCES

1. S. *Brenner* and *R. W. Horne, Biochem. Biophys. Acta—Prot. Struct.*, *34*, 103–110 (1959).
2. H. E. Huxley and *G.* Zubay, J. *Mol. Biol.*, *2*, 10–18 (1960).

3. A. Klug and J. E. Berger, J. Mol. Biol., **10, 565–569 (1964).**
4. D. J. DeRosier and A. Klug, Nature, **217,** 130–**134 (1968).**
5. W. Hoppe, R. Langer, G. Knesch, and C. Poppe, *Naturwissenschaften*, **55,333–336 (1968).**
6. **H.** P. Erickson and A. Klug, Philos. Trans. R. *Soc. Lond.* B, **261, 105–118** (1971).
7. P. N. T. Unwin and R. Henderson, *J.* Mol. Biol., **94,425440 (1975).**
8. J. Dubochet, J. Lepault, R. Freeman, J. A. Berriman, and J.-C. Homo, J. Microsc., **128,** 219–**237** (1982c).
9. J. Dubochet, M. Adrian, J.-J. Chang, J.-C. Homo, J. Lepault, A. W. McDowall, and P. Schultz, Q. Rev. Biophys., **21**, 129–228 **(1988).**
10. K. A. Taylor and R. M. Glaeser, Science, **186, 1036–1037 (1974).**
11. R. Henderson, J. M. Baldwin, T. A. Ceska, F. Zemlin, E. Beckmann, and K. H. Downing, J. Mol. Biol., **213, 899–929 (1990).**
12. W. Kuhlbrandt, D. N. Wang, and Y. Fujiyoshi, Nature, **367, 614–621 (1994).**
13. E. Nogales, S. G. Wolf, and K. H. Downing, Nature, **391, 199–203 (1998).**
14. K. Murata, K. Mitsuoka, T. Hirai, T. Waltz, P. Agre, J. B. Heymann, A. Engel, and Y. Fujiyoshi, Nature, **407,599–605 (2000).**
15. L. A. Amos, R. Henderson, and P. N. T. Unwin, Prog. Biophys. Mol. Biol., **39, 183–231 (1982).**
16. **T.** Walz & N. Grigorieff, J. Struct. Biol., **121, 142–161 (1998).**
17. **T.** S. Baker, N. H. Olson, and S. D. Fuller, *Mi*crobiol. Mol. Biol. Rev., **63,862–922 (1999).**
18. J. Frank, Three-Dimensional Electron Microscopy of *MacromolecularAssemblies*, Academic Press, San Diego, CA, **1996,342** pp.
19. I. Hargittai and M. Hargittai, Eds., *Stereo*chemical Applications of Gas-Phase Electron Diffraction, VCH, New York, **1988.**
20. **M.** Isaacson, J. Langmore, and H. Rose, Optik, **41**, 92–96 **(1974).**
21. R. Henderson, Q. Rev. Biophys., **28, 171–193** (1995).
22. W. A. Havelka, R. Henderson, and D. Oesterhelt, *J.* Mol. Biol., **247, 726–738 (1995).**
23. R. M. Glaeser, J. Ultrastruct. Res., **36,** 466–**482** (1971).
24. R. Henderson and P. N. T. Unwin, Nature, **257**, 28–32 **(1975).**
25. J. Frank, Curr. Opin. Struct. Biol., **7,266–272 (1997).**
26. J. Kenney, E. Karsenti, B. Gowen, and S. D. Fuller, J. Struct. Biol., **120, 320–328 (1997).**
27. Y. Tao, N. H. Olson, W. Xu, D. L. Anderson, M. G. Rossmann, and T. S. Baker, Cell, **95, 431–437 (1998).**
28. L. B. Kong, A. C. Siva, L. H. Rome, and P. L. Stewart, Structure, **7, 371–379 (1999).**
29. A. C. Bloomer, J. Graham, S. Hovmoller, P. J. G. Butler, and A. Klug, Nature, **276**, 362–**368 (1978).**
30. R. H. Jacobson, X.-J. Zhang, R. F. DuBose, and B. W. Matthews, Nature, **369,761–766** (1994).
31. G. P. A. Vigers, R. A. Crowther, and B. M. F. Pearse, EMBO J.,**5, 529–534 (1986).**
32. M. Schatz, E. V. Orlova, P. Dube, J. Jager, and M. van Heel, *J.* Struct. Biol., **114, 28–40 (1995).**
33. R. A. Grant, D. J. Filman, S. E. Finkel, R. Kolter, and J. M. Hogle, *Nat.* Struct. Biol., **5, 294–303 (1998).**
34. A. Mattevi, G. Obmolova, E. Schulze, K. H. Kalk, A. H. Westphal, A. D. Kok, and W. G. J. Hol, Science, **255, 1544–1550 (1992).**
35. R. A. Milligan, Proc. Natl. Acad. Sci. USA, **93, 21–26 (1996).**
36. A. Miyazawa, Y. Fujiyoshi, M. Stowell, and N. Unwin, J. Mol. Biol., **288, 765–786 (1999).**
37. K. Hirose, W. B. Amos, A. Lockhart, R. A. Cross, and L. A. Amos, *J.* Struct. Biol., **118, 140–148 (1997).**
38. K. Namba and F. Vonderviszt, Q. Rev. *Bio*phys., **30**, 1–65 **(1997).**
39. T.-W. Jeng, R. A. Crowther, G. Stubbs, and W. Chui, J. Mol. Biol., **205, 251–257 (1989).**
40. A. Cheng, A. N. van Hoek, M. Yeager, A. S. Verkman, and A. K. Mitra, Nature, **387, 627–630 (1997).**
41. V. M. Unger, N. M. Kumar, N. B. Gilula, and M. Yeager, Science, **283,1176–1180 (1999).**
42. D. A. Winkelmann, T. S. Baker, and I. Rayment, J. Cell Biol., **114, 701–713** (1991).
43. K. A. Taylor, J. Tang, Y. Cheng, and H. Winkler, J. Struct. Biol., **120,372–386 (1997).**
44. B. Bottcher, S. A. Wynne, and R. A. Crowther, Nature, **386, 88–91 (1997).**
45. A. Malhotra, P. Penczek, R. K. Agrawal, I. S. Gabashvili, R. A. Grassucci, R. Junemann, N. Burkhardt, K. H. Nierhaus, and J. Frank, J. Mol. Biol., **280, 103–116 (1998).**
46. **R.** W. Horne and I. Pasquali-Ronchetti, J. *Ul*trastruct. Res., **47, 361–383 (1974).**

47. H. Yoshimura, M. Matsumoto, S. Endo, and K. Nagayama, *Ultramicroscopy,* 32, 265-274 (1990).

48. R. Kornberg and S. A. Darst, *Curr. Opin. Struct. Biol.,* 1,642-646 (1991).

49. B. Jap, M. Zulauf, T. Scheybani, A. Hefti, W. Baumeister, and U. Aebi, *Ultramicroscopy,* 46, 45-84(1992).

50. E. W. Kubalek, S. F. J. LeGrice, and P. O. Brown, J. *Struct. Biol.,* 113,117-123(1994).

51. J.-L. Rigaud, G. Mosser, J.-J. Lacapere, A. Olofsson, D. Levy, and J.-L. Ranck, J. *Struct. Biol.,* 118, 226-235(1997).

52. L. Hasler, J. B. Heymann, A. Engel, J. Kistler, and T. Walz, *J. Struct. Biol.,* 121, 162-171 (1998).

53. I. Reviakine, W. Bergsma-Schutter, and A. Brisson, J. *Struct. Biol.,* 121, 356-361(1998).

54. E. M. Wilson-Kubalek, R. E. Brown, H. Celia, and R. A. Milligan, *Proc. Natl. Acad. Sci. USA,* 95, 8040-8045(1998).

55. A. Polyakov, C. Richter, A. Malhotra, D. Koulich, S. Borukhov, and S. A. Darst, J. *Mol. Biol.,* 281, 465-473(1998).

56. M. Adrian, J. Dubochet, J. Lepault, and A. W. McDowall, *Nature,* 308, 32–36(1984).

57. J. R. Bellare, H. T. Davis, L. E. Scriven, and Y. Talmon, J. *Electron Microsc. Technol.,* 10, 87–111(1988).

58. E. Mayer and G. Astl, *Ultramicroscopy,* 45, 185-197(1992).

59. J. Berriman and N. Unwin, *Ultramicroscopy,* 56, 241-252(1994).

60. H. D. White, M. L. Walker, and J. Trinick, *J. Struct. Biol.,* 121, 306–313(1998).

61. S. Subramaniam, M. Gerstein, D. Oesterhelt, and R. Henderson, *EMBO J.,* 12, 1–18(1993).

62. D. P. Siegel, W. J. Green, and Y. Talmon, *Biophys. J.,* 66, 402-414(1994).

63. S. Trachtenberg, *J. Struct. Biol.,* 123, 45-55 (1998).

64. N. Unwin, *Nature,* 373, 37–43(1995).

65. S. D. Fuller, J. A. Berriman, S. J. Butcher, and B. E. Gowen, *Cell,* 81, 715-725(1995).

66. D. P. Siegel and R. M. Epand, *Biophys.* J., 73, 3089-3111(1997).

67. M. Walker, X.-Z Zhang, W. Jiang, J. Trinick, and H. D. White, *Proc. Natl. Acad. Sci. USA,* 96, 465-470(1999).

68. M. Cyrklaff and W. Kiihlbrandt, *Ultramicroscopy,* 55, 141-153(1994).

69. J. C. H. Spence, *Experimental High-Resolution Electron Microscopy,* Oxford University Press, Oxford, UK, 1988.

70. L. Reimer, *Transmission Electron Microscopy,* Springer-Verlag, Berlin, 1989.

71. R. H. Wade and J. Frank, *Optik,* 49, 81-92 (1977).

72. R. H. Wade, *Ultramicroscopy,* 46, 145-156 (1992).

73. C. Toyoshima, K. Yonekura, and H. Sasabe, *Ultramicroscopy,* 48, 165-176(1993).

74. R. H. Cheng, N. H. Olson, and T. S. Baker, *Virology,* 186, 655–668(1992).

75. B. L. Trus, R. B. S. Roden, H. L. Greenstone, M. Vrhel, J. T. Schiller, and F. P. Booy, *Nat. Struct. Biol.,* 4, 413-420(1997).

76. F. Zemlin, *Ultramicroscopy,* 46, 25–32(1992).

77. Z. H. Zhou and W. Chiu, *Ultramicroscopy,* 49, 407-416(1993).

78. F. Zemlin, *Micron,* 25, 223-226(1994).

79. E. J. Mancini, F. D. Haas, and S. D. Fuller, *Structure,* 5, 741-750(1997).

80. J. Brink, M. B. Sherman, J. Berriman, and W. Chiu, *Ultramicroscopy,* 72, 41–52(1998).

81. O. L. Krivanek and P. E. Mooney, *Ultramicroscopy,* 49, 95–108 (1993).

82. M. B. Sherman, J. Brink, and W. Chiu, *Micron,* 27, 129-139(1996).

83. D. J. DeRosier and P. B. Moore, *J. Mol. Biol.,* 52, 355-369(1970).

84. J. L. Carrascosa and A. C. Steven, *Micron,* 9, 199-206(1978).

85. M. van Heel and J. Frank, *Ultramicroscopy,* 6, 187-194(1981).

86. I. S. Gabashvili, R. K. Agrawal, C. M. T. Spahn, R. A. Grassucci, D. I. Svergun, J. Frank, and P. Penczek, *Cell,* 100, 537-549(2000).

87. M. Radermacher, T. Wagenknecht, A. Verschoor, and J. Frank, *J. Microsc.,* 146, 113-136 (1987).

88. M. Radermacher, J. *Electron Microsc. Technol.,* 9, 359-394 (1988).

89. J. Frank, M. Radermacher, P. Penczek, J. Zhu, Y. Li, M. Ladjadj, and A. Leith, *J. Struct. Biol.,* 116, 190-199(1996).

90. M. van Heel, *Ultramicroscopy,* 21, 111-124 (1987a).

91. M. van Heel, G. Harauz, and E. V. Orlova, *J. Struct. Biol.,* 116, 17-24(1996).

92. M. Radermacher in D.-P. Hader, Ed., *Image Analysis in Biology,* CRC Press, Boca Raton, FL, 1991, pp. 219-246.

93. *M. Radermacher in J. Frank, Ed., Electron Tomography, Plenum Press, New York,* **1992,** *pp.* **91-115.**

94. *M. Radermacher, Ultramicroscopy,* **53, 121-136 (1994).**

95. *P. A. Penczek, R. A. Grassucci, and J. Frank, Ultramicroscopy,* **53, 251-270 (1994).**

96. *M. Schatz and M. van Heel, Ultramicroscopy,* **32, 255-264 (1990).**

97. *P. Penczek, M. Radermacher, and J. Frank, Ultramicroscopy,* **40,** 33–53 **(1992).**

98. *N. Grigorieff,* **J.** *Mol. Biol.,* **277, 1033-1046** (1998).

99. *D.* **E.** *Olins, A. L. Olins, H. A. Levy, R. C. Durfee, S.* **M.** *Margle, E. P. Tinnel, and S. D. Dover, Science,* **220, 498-500** (1983).

100. *U. Skoglund and B. Daneholt, Trends Biochem. Sci.,* **11, 499503 (1986).**

101. *J. C. Fung, W. Liu, W. J.* **DeRuijter,** *H. Chen, C. K. Abbey, J. W. Sedat, and D. A. Agard, J. Struct. Biol.,* **116, 181-189** (1996).

102. *W. Baumeister, R. Grimm, and J. Walz, Trends Cell Biol.,* **9,** 81–85 **(1999).**

103. *A. K. Shah and P. L. Stewart, J. Struct. Biol.,* **123, 17-21 (1998).**

104. *F. Beuron, M. R. Maurizi, D. M. Belnap, E. Kocsis, F. P. Booy, M. Kessel, and A. C. Steven, J. Struct. Biol.,* **123, 248-259** (1998).

105. *R. A. Crowther, L. A. Amos, J. T. Finch, D. J. DeRosier, and A.* **Klug,** *Nature,* **226, 421-425 (1970).**

106. *R. A. Crowther, Philos. Trans. R. Soc. Lond.,* **261, 221-230 (1971).**

107. *S. D. Fuller, S. J. Butcher, R. H. Cheng, and T. S. Baker, J. Struct. Biol.,* **116,** 48–55 **(1996).**

108. *R. H. Cheng, V. S. Reddy, N. H. Olson, A. J. Fisher, T. S. Baker, and J. E. Johnson, Structure,* **2, 271-282 (1994).**

109. *R. A. Crowther, N. A. Kiselev, B. Bottcher, J. A. Berriman, G. P. Borisova, V. Ose, and P.* **Pumpens,** *Cell,* **77, 943-950 (1994).**

110. *T. S. Baker and R. H. Cheng, J. Struct. Biol.,* **116, 120-130 (1996).**

111. *J. R.* **Castón,** *D. M. Belnap, A. C. Steven, and B. L. Trus, J. Struct. Biol.,* **125, 209-215** (1999).

112. *R. A. Crowther, R. Henderson, and J. M. Smith, J. Struct. Biol.,* **116, 9-16 (1996).**

113. *J. A.* **Lawton** *and B. V. V.* **Prasad,** *J. Struct. Biol.,* **116, 209-215 (1996).**

114. *P. A. Thuman-Commike and W. Chiu, J. Struct. Biol.,* **116, 41-47 (1996).**

115. **I.** *M. Boier Martin, D. C.* **Marinescu,** *R. E. Lynch, and T. S. Baker, J. Struct. Biol.,* **120, 146-157 (1997).**

116. *Z. H. Zhou, W. Chiu, K. Haskell, H. J. Spears, J. Jakana, F. J. Rixon, and L. R. Scott, Biophys.* **J., 74, 576-588 (1998).**

117. **P.** *L. Stewart, C. Y. Chiu, S. Huang, T.* **Muir, Y.** *Zhao, B. Chait, P.* **Mathias,** *and G. R.* **Nemerow,** *EMBO J.,* **16, 1189-1198 (1997).**

118. *J. Walz, T. Tamura, N. Tamura, R. Grimm, W. Baumeister, and A. J. Koster, Mol. Cell,* **1, 59-65 (1997).**

119. *M. Stewart,* **J.** *Electron Microsc. Technol.,* **9, 325-358 (1988).**

120. *C. Toyoshima and N. Unwin, J. Cell Biol.,* **111, 2623-2635 (1990).**

121. *D. G. Morgan and D. DeRosier, Ultramicroscopy,* **46, 263-285** (1992).

122. *N. Unwin,* **J.** *Mol. Biol.,* **229, 1101-1124** (1993).

123. *R. Beroukhim and N. Unwin, Ultramicroscopy,* **70, 57-81** (1997).

124. **E. H.** *Egelman, Ultramicroscopy,* **19,** 367–374 (1986).

125. *B. Carragher, M. Whittaker, and R. A.* **Milligan,** *J. Struct. Biol.,* **116, 107-112** (1996).

126. *C. H. Owen, D. G. Morgan, and D. J. DeRosier, J. Struct. Biol.,* **116, 167-175 (1996).**

127. *R. Henderson, J. M.* **Baldwin,** *K. H. Downing, J.* **Lepault,** *and F. Zemlin, Ultramicroscopy,* **19,** 147–178 **(1986).**

128. *J. M.* **Baldwin,** *R. Henderson, E.* **Beckman,** *and F. Zemlin, J. Mol. Biol.,* **202, 585-591 (1988).**

129. *S. Hardt, B.* **Wang, and M.** *F. Schmid, J. Struct. Biol.,* **116, 68-70 (1996).**

130. *R. A. Crowther and P. K. Luther, Nature,* **307, 569-570 (1984).**

131. *H. Winkler and K. A. Taylor, J. Struct. Biol.,* **116, 241-247 (1996).**

132. **J.** *Frank in J. Frank,* Ed., *Electron Tomography: Three-Dimensional Imaging with the Transmission Electron Microscope, Plenum Press, New York,* **1992, 399** *pp.*

133. *J. Frank, A. Verschoor, and M. Boublik, Science,* **214, 1353-1355 (1981).**

134. *M. van Heel, Ultramicroscopy,* **21, 95-100** (1987b).

135. *M. van Heel and J. Hollenberg in W.* **Baumeister** *and W. Vogell, Eds., Electron Microscopy at Molecular Dimensions, Springer-Verlag, Berlin,* **1980,** *pp.* **256-260.**

136. *M. Unser, B. L. Trus, J. Frank, and A. C. Steven, Ultramicroscopy,* **30, 429-434** (1989).

137. D. A. Agard, *J.* Mol. Biol., **167, 849-852 (1983).**

138. J. M. Valpuesta, J. L. Carrascosa, and R. Henderson, *J.* Mol. Biol., **240, 281-287 (1994).**

139. J. T. Finch, *J.* Mol. Biol., **66, 291-294 (1972).**

140. Z. H. Zhou, S. Hardt, B. Wang, M. B. Sherman, J. Jakana, and W. Chiu, J. Struct. Biol., **116, 216-222 (1996).**

141. N. H. Olson and T. S. Baker, Ultramicroscopy, **30, 281-298 (1989).**

142. D. M. Belnap, N. H. Olson, and T. S. Baker, *J.* Struct. Biol., **120, 44-51 (1997).**

143. Y. Fujiyoshi, T. Mizusaki, K. Morikawa, H. Yamagishi, Y. Aoki, H. Kihara, and Y. Harada, Ultramicroscopy, **38, 241-251 (1991).**

144. F. Zemlin, E. Beckmann, and K. D. vander-Mast, Ultramicroscopy, **63, 227-238 (1996).**

145. N. Kisseberth, M. Whittaker, D. Weber, C. S. Potter, and B. Carragher, *J.* Struct. Biol., **120, 309-319 (1997).**

146. M. Hadida-Hassan, S. J. Young, S. T. Peltier, M. Wong, S. Lamont, and M. H. Ellisman, *J.* Struct. Biol., **125, 235-245 (1999).**

147. B. F. McEwen, K. H. Downing, and R. M. Glaeser, *Ultramicroscopy*, **60,** 357–373 **(1995).**